# Turbulence-Driven Edge-Localized-Mode-Free High-Confinement Mode with Divertor Detachment in a Metal-Wall Tokamak

G. S. Xu,[1,*] G. F. Ding,[1] G. J. Zhang,[1,2] Y. F. Wang,[1] X. Jian,[1] T. Zhang,[1] Z. Q. Zhou,[1,2] K. Wu,[1] Q. Q. Yang,[1] R. Chen,[1] L. Yu,[1,2] L. Y. Meng,[1] L. Wang,[1] H. Q. Wang,[3] N. M. Li,[4] Z. Y. Lu,[1] K. D. Li,[1] S. Y. Ding,[3] N. Yan,[1] L. Q. Xu,[1] X. Lin,[1] B. Zhang,[1] J. P. Qian,[1] T. F. Zhou,[1] P. Li,[1] C. Zhou,[2] S. F Wang,[2] Q. Zang,[1] H. Q. Liu,[1] F. Ding,[1] L. Zhang,[1] Y. F. Jin,[1] Y. M. Duan,[1] Y. W. Yu,[1] R. Ding,[1] G. Q. Li,[1] X. Z. Gong,[1] K. Lu,[1] J. S. Hu,[1] Y. T. Song,[1] and B. N. Wan[1,†]

[1]*Institute of Plasma Physics, Hefei Institutes of Physical Science, Chinese Academy of Sciences, Hefei 230031, China*
[2]*University of Science and Technology of China, Hefei 230026, China*
[3]*General Atomics, P.O. Box 85608, San Diego, California 92186-5608, USA*
[4]*Lawrence Livermore National Laboratory, Livermore, California 94550, USA*

(Received 31 October 2025; revised 27 December 2025; accepted 17 February 2026; published 23 March 2026)

We report the first demonstration of a minute-scale, edge-localized-mode-free high-confinement plasma regime compatible with divertor partial detachment and enhanced pedestal performance in a metal-wall tokamak, the Experimental Advanced Superconducting Tokamak. This regime is enabled by a newly identified mechanism: during divertor partial detachment, reduced ionization and enhanced pumping in a closed divertor lead to less cooling of the pedestal by recycling neutrals and seeding impurities, resulting in an increased pedestal temperature gradient, which excites high-frequency broadband turbulence. Gyrokinetic simulations identify the high-frequency broadband turbulence as a temperature-gradient-driven trapped electron mode ($\eta_e$-TEM), which drives outward transport of particles and heat, thereby maintaining the edge-localized-mode-free state. This pedestal regime is particularly promising for the International Thermonuclear Experimental Reactor, where the anticipated lower density gradient, reduced E × B shear, and lower collisionality in the pedestal will further facilitate $\eta_e$-TEM excitation. The achieved integrated scenario with a detached divertor and turbulence-dominated pedestal thus offers a compelling solution for managing heat loads and metal impurity sources for long-pulse high-performance operation in future fusion reactors.

DOI: 10.1103/7r3f-dqft

A key challenge for next-step fusion devices such as the International Thermonuclear Experimental Reactor (ITER) [1] is handling the intense heat flux toward the divertor. Without effective mitigation, the heat load on the divertor target plates in a reactor would exceed material limits, causing material erosion and damage. Divertor detachment, enabled by low-Z impurity seeding to enhance radiative cooling and drastically reduce target plate heat flux, is the leading strategy for divertor power handling. Yet, deep or complete detachment across the full extent of divertor target plates [2] is typically accompanied by the migration of the radiation zone into the pedestal region, which degrades pedestal performance by cooling the pedestal plasma [3]. Here, the pedestal refers to a narrow region with a steep pressure gradient at the plasma edge in the so-called high-confinement mode (H mode) [4]. Thus, a plasma regime capable of achieving compatibility between divertor detachment and high pedestal performance is highly desirable.

H-mode plasmas are prone to repetitive edge instabilities known as edge-localized modes (ELMs) [5], which expel bursts of energy and particles. Large ELMs with a substantial loss of plasma stored energy would cause unacceptable erosion and damage to plasma-facing components. The resulting erosion generates metallic impurities that contaminate the core plasma, degrade overall performance, and hinder stable operation, particularly in the full-metal wall environment planned for ITER [1]. Therefore, an ideal regime for future reactors would be a stationary, ELM-free, H-mode plasma with high pedestal performance that is simultaneously coupled with divertor detachment. The key to accessing this regime typically requires a radial transport channel across the pedestal to limit pedestal growth and prevent it from exceeding the stability boundary, thereby

*Contact author: gsxu@ipp.ac.cn
†Contact author: bnwan@ipp.ac.cn

*Published by the American Physical Society under the terms of the Creative Commons Attribution 4.0 International license. Further distribution of this work must maintain attribution to the author(s) and the published article's title, journal citation, and DOI.*

avoiding ELMs [6]. Turbulence can provide such a transport channel.

Recently, short periods of ELM-free H mode with divertor detachment have been achieved through impurity seeding in tokamaks such as AUG [7,8], DIII-D [9,10], and JET [11]. However, a general degradation of pedestal performance has been observed with reductions in pedestal temperature and pressure. In particular, the recently developed X-point radiator divertor regime, typically requires substantial impurity seeding, accompanied by divertor deep detachment and a reduction of pedestal height [8,12]. If a plasma regime could achieve detached ELM-free H mode without degradation of pedestal performance, it would be highly desirable for ITER and future reactors. In this Letter, we report the first discovery of such a plasma regime and demonstrate its sustained operation at minute scale in recent experiments on the Experimental Advanced Superconducting Tokamak (EAST) with a boronized full-metal wall. By revealing the underlying physics, we predict its feasibility for the ITER, paving the way for its application in future reactors. The ITER has decided to switch its plasma-facing wall material from beryllium to tungsten, with boronization for wall conditioning, and using electron cyclotron resonance heating (ECRH) to control tungsten impurity concentration in the plasma [13]. The ITER particularly needs such an operational regime to address the challenge of long-pulse, high-performance operations with full-metal walls. The EAST now has ITER-like conditions, i.e., boronized full-metal wall and high-power ECRH heating. Although the EAST cannot match all normalized parameters of the ITER, such as collisionality, the EAST results could offer valuable insights for the ITER.

Our experimental results on the EAST demonstrate that the increased neutral pressure from partial detachment in a relatively closed divertor enhances pumping. This reduces pedestal cooling by recycling neutrals and seeding impurities, thus increasing the pedestal temperature gradient, which excites the newly observed high-frequency broadband turbulence (HFBT) in the pedestal gradient region. Unlike previously reported edge coherent modes on the EAST [14,15], HFBT has been observed in the pedestal at low collisionality. Gyrokinetic simulations identify HFBT as a temperature-gradient-driven trapped electron mode ($\eta_e$-TEM) [16], providing a continuous transport channel across the pedestal that suppresses ELMs and prevents impurity accumulation. This ELM-free H mode with detached divertor and turbulence-dominated pedestal, termed the "DTP" regime, offers a promising regime for long-pulse, high-performance, stable operation under full-metal wall conditions for the ITER and future reactors.

More recently, a strikingly similar ELM-free H mode has been observed in high-power deuterium-tritium experiments on the JET tokamak at low $q_{95}$ (~3) and low pedestal-top collisionality $\nu^*_{e,\mathrm{top}}$ (~0.5) in an ITER-like configuration with neon impurity seeding in the divertor [17]. A drop in pedestal density along with a significant temperature increase was recorded, although measurements of pedestal fluctuations were unfortunately lacking. Should the underlying physical mechanism be identical, it would imply that this regime holds significant promise for application in future large-scale tokamaks.

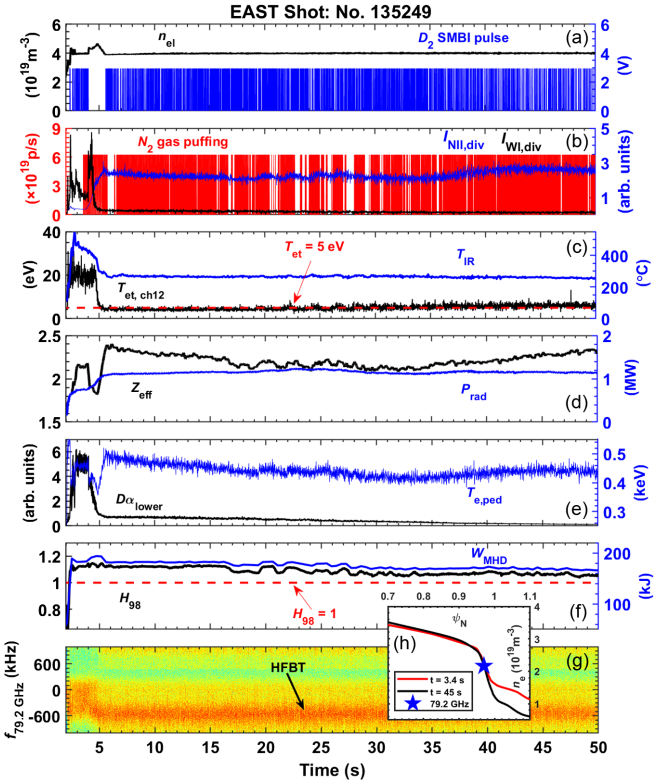



FIG. 1. (a) Central line-averaged electron density measured by a polarimeter or interferometer (black) and deuterium SMBI pulses for density feedback control (blue). (b) $N_2$ injection rate from the lower divertor with pulse width modulation (red), nitrogen NII (blue) line emissions from the lower divertor, and tungsten WI (black) line emission from the lower divertor. (c) Electron temperature measured by divertor Langmuir probe channel 12 and divertor peak surface temperature measured by an infrared camara (blue). (d) Effective charge number (black) and radiation power of the bulk plasma measured by bolometer arrays (blue). (e) D$\alpha$ line emission from the lower divertor (black) and electron temperature near the pedestal top measured by electron cyclotron emission (ECE) (blue). (f) Energy confinement enhancement factor (black) and plasma stored energy (blue). (g) Frequency spectrum measured by a channel of the MPCR at 79.2 GHz. (h) Electron density profiles measured by a sweep-frequency reflectometer with the blue star indicating the location of the MPCR channel at 79.2 GHz.

The EAST has achieved for the first time long-pulse (50–70 s) operations of the DTP regime via feedback-controlled divertor nitrogen ($N_2$) seeding with a boronized full-metal wall. Figure 1 shows such a typical discharge (No. 135249) of 50 s (limited by central solenoid flux consumption) with a toroidal magnetic field $B_t = 2.45$ T in the favorable

direction for the lower single-null divertor configuration, plasma current $I_p = 0.4$ MA and $q_{95} = 6.2$, where $q_{95}$ is the safety factor at the 95% poloidal flux surface. The injected power ($P_{\rm inj}$) is 4.3 MW, including 2.4 MW ECRH and 1.9 MW lower-hybrid current drive. The power transported across the separatrix, $P_{\rm sep}$, is about 3.6 MW, which is ~2.2 times of the L-H transition threshold power ($P_{\rm L-H}$) [18]. Here, $P_{\rm sep} = P_{\rm inj} - P_{\rm rad}$, where $P_{\rm rad}$ is the radiation power of the bulk plasma. The central line-averaged electron density ($n_{\rm el}$) was maintained stably at $4 \times 10^{19}$ m$^{-3}$ (~61% of the Greenwald density) through feedback control with supersonic molecular beam injection (SMBI) from the outer midplane [Fig. 1(a)]. The energy confinement enhancement factor $H_{98y2}$ was maintained at ~1.1 during the whole discharge [Fig. 1(f)]. Stable detachment at both the inner and outer target plates of the lower divertor was achieved by feedback control of the electron temperature ($T_{\rm et}$) at the outer target plate of the lower divertor [19]. The $T_{\rm et}$ near the lower outer divertor strike point was reduced to ~5 eV and the divertor peak surface temperature was reduced from ~500 °C to ~250 °C [Fig. 1(c)]. The tungsten impurity source from the divertor was significantly suppressed, as indicated by the tungsten WI line emission from the lower divertor [Fig. 1(b)]. The effective charge number $Z_{\rm eff}$ was maintained at ~2.2. The divertor D$\alpha$ signal dropped sharply when $N_2$ seeding started and then continued to decrease [Fig. 1(e)], while the scrape-off layer (SOL) density significantly decreased as well [Fig. 1(h)]. Here, the $\psi_N$ in Fig. 1(h) is the normalized poloidal magnetic flux. The pedestal top density did not show a significant decrease due to the SMBI feedback control, while the pedestal top electron temperature significantly increased at the onset of divertor partial detachment [Fig. 1(e)]. In this long-pulse ELM-free discharge, the HFBT was observed in the pedestal gradient region with a frequency of about 350 kHz before $N_2$ seeding, as measured by a channel at 79.2 GHz of the multichannel poloidal correlation reflectometer (MPCR) [20], and then shifted upwards to ~550 kHz during $N_2$ seeding [Fig. 1(g)].

The DTP regime with significantly enhanced confinement has been obtained at a lower $q_{95}$ in short pulses. Figure 2 shows a typical discharge (No. 133903) in the EAST featuring simultaneous ELM suppression, enhanced energy confinement, and divertor detachment via feedback-controlled $N_2$ seeding, heated by 2.8 MW ECRH in a lower-biased double null configuration with $B_t = 2.45$ T, $I_p = 0.5$ MA, and $q_{95} = 5.2$. Different from the long-pulse discharge (No. 135249), the short-pulse discharge begins at a relative low confinement with $H_{98y2} \sim 0.85$ due to a lower $P_{\rm sep}$, which is 1.2 times of $P_{\rm L-H}$. This $P_{\rm sep}/P_{\rm L-H}$ ratio is close to the design values of future fusion reactors, such as the ITER, which is typically slightly greater than 1 to minimize the challenges posed by divertor heat loads. The outer strike point of the lower divertor was located at the horizontal target plate as shown in Fig. 2(k). $N_2$ was injected from the outer horizontal target plate of the lower

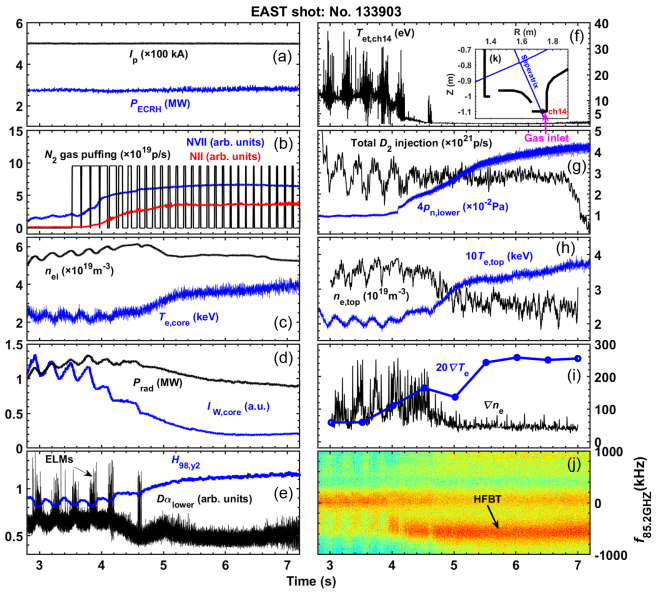



FIG. 2. (a) Plasma current (black) and ECRH injected power (blue). (b) Nitrogen injection rate from the lower divertor with pulse width modulation (black), nitrogen NVII line emission from the plasma core measured by an extreme ultraviolet spectrometer (blue) and nitrogen NII line emission from the lower divertor (red). (c) Central line-averaged electron density (black) and electron temperature on axis (blue) measured by ECE. (d) Radiation power of the bulk plasma (black) and tungsten line emission from the plasma core measured by an extreme ultraviolet spectrometer (blue). (e) D$\alpha$ line emission from the lower divertor (black) and energy confinement enhancement factor (blue). (f) Electron temperature near the strike point measured by divertor Langmuir probe channel 14 at the horizontal target plate. (g) Total deuterium gas injection rate (black) and neutral pressure (blue) measured by a pressure gauge installed on the lower port. (h) Electron density (black) measured by a sweep-frequency reflectometer and electron temperature (blue) measured by ECE in the pedestal top region at $\psi_N \sim 0.95$. (i) Peak electron density gradient (black) measured by sweep-frequency reflectometer and peak electron temperature gradient (blue) measured by Thomson scattering of the pedestal region. (j) Frequency spectra measured by a channel of the MPCR at 85.2 GHz. (k) The locations of the divertor strike points and divertor Langmuir probe channel 14.

divertor near the right-angle closed corner into the SOL. The $T_{\rm et}$ measured by divertor target Langmuir probes was initially used to detect the onset of detachment. Then, the system switched to feedback control of one channel of the absolute extreme ultraviolet radiation signal near the lower X point with seeding pulse width modulation to maintain detachment [21].

Partial detachment was achieved at the lower outer divertor with $T_{\rm et}$ near the strike point being reduced to $< 2$ eV, but in the far SOL the vertical target plates were still attached [Fig. 3(f)]. The heat flux was reduced to a low level over the entire area of the target plates [Fig. 3(h)]. When the outer strike point is located on the horizontal

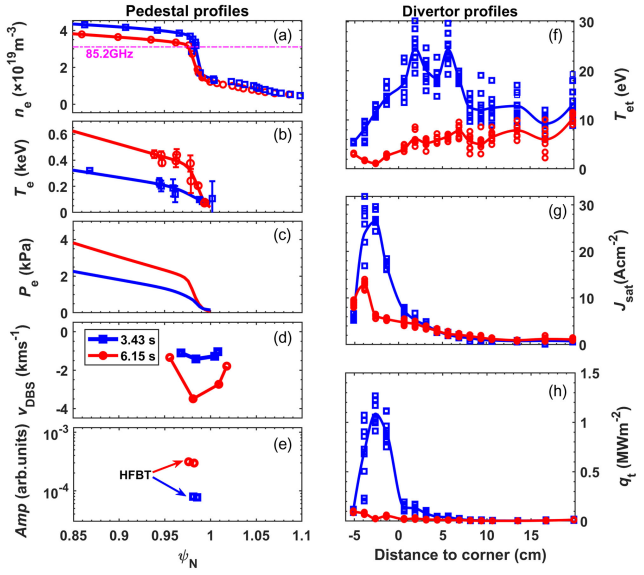



FIG. 3. (a) Electron density profiles measured by the sweep-frequency reflectometer. (b) Electron temperature profiles measured by Thomson scattering. (c) Electron pressure profiles. (d) Perpendicular propagation velocity measured by Doppler backscattering. (e) Amplitude of HFBT calculated from MPCR. (f)–(h) Divertor electron temperature, particle flux, and vertical heat flux measured by divertor Langmuir probes, at 3.43 s (blue) and 6.15 s (red), of the EAST discharge No. 133903.

target plate, the right-angle closed corner divertor structure of the EAST helps to confine recycling neutrals through target-plate reflection [22], thereby reducing $T_{\mathrm{et}}$ near the strike point. Therefore, before $N_2$ seeding, the $T_{\mathrm{et}}$ profile peaked on the vertical target plate (Fig. 3).

Prior to $N_2$ seeding, large ELMs causing a 2%–4% loss of the plasma stored energy appeared intermittently, as indicated by the divertor D$\alpha$ and $T_{\mathrm{et}}$ signals [Figs. 2(e) and 2(f)]. With $N_2$ seeding, the duration of ELM-free periods extended progressively. Finally, ELMs were completely suppressed when divertor detachment was achieved at the lower outer divertor. The divertor neutral pressure significantly increased, starting around 4.1 s at the onset of divertor detachment [Fig. 2(g)], which enhanced the pumping of recycling neutrals, while the external deuterium gas fueling rate remained nearly constant [Fig. 2(b)]. The increased neutral pressure could be caused by the reduction in ionization of recycling neutrals due to the "power starvation" effect [23], that is, the detachment leads to a decrease in the energy flowing into the area near the divertor target plates. The enhanced pumping may lead to less fueling of the pedestal by recycling neutrals and seeding impurities, and thus less cooling of the pedestal, which results in a decrease in the pedestal density [Fig. 2(h) and 3(a)] and a significant increase in the pedestal electron temperature $T_e$ [Fig. 2(h)] and $T_e$ gradient [Figs. 2(i) and 3(b)]. As a result, the $n_{\mathrm{el}}$ decreased and $T_e$ at the plasma center significantly increased [Fig. 2(c)]. The pedestal top pressure approximately doubles compared to the attached phase prior to $N_2$ seeding [Fig. 3(c)]. The plasma energy confinement was improved, as indicated by the $H_{98y2}$ factor, which gradually increased and finally reached 1.2 [Fig. 2(e)]. In addition, the perpendicular propagation velocity in the pedestal region measured by Doppler backscattering [24] becomes much more negative in the electron diamagnetic direction [Fig. 3(d)]. This suggests that the $\mathrm{E}\times\mathrm{B}$ velocity and ion temperature gradient increased significantly, as the perpendicular propagation velocity is usually dominated by $\mathrm{E}\times\mathrm{B}$ velocity in the pedestal and related to the ion temperature gradient through radial force balance. Moreover, radiation from metallic impurities (tungsten, molybdenum, copper, and iron) and the total radiated power decreased significantly [Fig. 2(d)], which could be a result of suppression of the impurity source. The key requirement for sustaining this regime is to maintain a sufficient divertor radiation level to keep the divertor in a partial detachment state, while simultaneously avoiding excessive radiation near the divertor X point that would cool the pedestal plasma. Thus, this has to be achieved through feedback control. Comparison experiments have shown that excessive nitrogen impurity injection leads to enhanced radiation near the divertor X point, resulting in an increase in pedestal density and a degradation in pedestal performance.

Pedestal linear stability analysis using the elite code [25] indicates that prior to $N_2$ seeding the pedestal is in the deeply stable region of the ideal Peeling-Ballooning mode, far from the corner region where type I ELMs are typically triggered. However, BOUT++ simulations [26] suggest that the resistive-ballooning mode is still unstable, which may be responsible for the ELM occurrence in the experiment. During $N_2$ seeding, the elite code shows that the pedestal is close to the corner between the peeling boundary and the ballooning boundary, but still in the stable region. To maintain the pedestal near the instability boundary for long-pulse operation, it is necessary to have a transport channel across the pedestal to prevent further growth beyond the instability boundary, which can be provided by turbulence.

Prior to $N_2$ seeding, the HFBT was detected by the 85.2 GHz channel of an MPCR in the upper region of the pedestal with a frequency of 200–500 kHz, though with rather weak amplitude [Fig. 2(j)]. The radial position of the MPCR channel is shown in Fig. 3(a). During $N_2$ seeding, the HFBT amplitude significantly increased [Fig. 3(e)] and its frequency was upshifted to 400–700 kHz, which could be due to the Doppler shift. The HFBT was not visible to the high-frequency Mirnov coils, suggesting that it could be an electrostatic mode. The HFBT propagates in the electron diamagnetic drift direction in the laboratory frame. The poloidal wave number $k_y$ of the HFBT is estimated to be about 0.59 $\mathrm{mm}^{-1}$ through poloidal correlation analysis based on the MPCR measurement. Given the local ion gyroradius at the ion sound speed, $\rho_s = c_s/\omega_{ci} \sim 1.44$ mm,

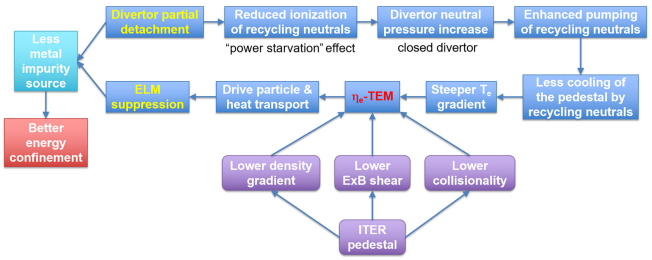



FIG. 4. A schematic diagram showing the principle of the DTP regime.

we thus obtain $k_y\rho_s \sim 0.85$, where $c_s = \sqrt{T_e/m_i}$ is the ion sound speed and $\omega_{ci} = eB/m_i$ is the ion cyclotron frequency with $m_i$ being the deuterium ion mass and $B$ being the magnetic field strength. From the parameter time evolution [Figs. 2(h)–2(j)], we find that the amplitude of the HFBT increases with increasing pedestal electron temperature gradient and decreasing $\nu^*_{e,\mathrm{top}}$. The HFBT has also been observed in the EAST experiments with much lower pedestal collisionality ($\nu^*_{e,\mathrm{top}} < 1$). These experiments were conducted without impurity seeding, in which the HFBT existed in the intervals between small ELMs and was not associated with ELM suppression so far.

In order to understand the nature of the HFBT, local linear and nonlinear gyrokinetic simulations of the pedestal are performed using the high-fidelity code GENE [27]. The linear simulation results, shown in End Matter Fig. 5, indicate the presence of an $\eta_e$-TEM in the pedestal gradient region in the intermediate $k_y\rho_s = 0.6$–$1.2$ range during $N_2$ seeding, which is destabilized by temperature gradient and stabilized by collisionality, in good agreement with most features of the observed HFBT. Furthermore, nonlinear simulations show that this mode drives radially outward particle and electron heat fluxes, providing a radial transport channel across the pedestal, which may be responsible for the ELM suppression.

As illustrated in the schematic diagram of Fig. 4, the underlying principle of the DTP regime can be summarized as follows. During divertor partial detachment, the power flow to the closed divertor is significantly reduced. This results in decreased ionization of recycling neutral particles due to the "power starvation" effect [23]. Consequently, the divertor neutral pressure rises, and the pumping efficiency for recycling neutrals is enhanced, leading to reduced cooling of the pedestal by recycling neutrals, and thus an increase in the pedestal $T_e$ gradient, which favors the excitation of $\eta_e$-TEM. According to gyrokinetic simulations, such turbulence drives outward transport of particles and heat, which suppresses ELMs and sustains an ELM-free state. As a result of divertor detachment and ELM suppression, the metal impurity source is significantly reduced, which may be responsible for the improved global energy confinement. A closed divertor configuration is a necessary condition for constraining recycling neutral particles and seeding impurities within the divertor region, thereby preventing them from easily penetrating the pedestal region. In contrast, in the X-point radiator divertor regime characterized by deep detachment [12] or seeding with higher-Z impurities, i.e., neon and argon on the EAST [33], the pedestal temperature always decreases, and the DTP regime has never been observed. This is because recycling neutrals and seeding impurities have penetrated to the vicinity of the divertor X point, significantly cooling the pedestal. On the EAST, the DTP regime is observed only with $N_2$ seeding. This is because the relatively low ionization potential of $N_2$ leads to it ionizing predominantly within the divertor region. In contrast, on JET, despite the higher ionization potential of neon, the much higher pedestal temperature and density allow it to still ionize mainly in the divertor, enabling the DTP regime with neon seeding [17].

Because of the unfavorable scaling of the turbulence suppression by $\mathrm{E}\times\mathrm{B}$ flow shear on the normalized ion gyroradius, $\rho^*$, turbulence suppression in the ITER pedestal is expected to be significantly weaker [34,35]. Therefore, the ITER pedestal would be more prone to low-wave number and intermediate-wave number turbulence, particularly TEM and ion temperature gradient modes, which are usually suppressed by strong $\mathrm{E}\times\mathrm{B}$ flow shear in the pedestal of present tokamaks. Furthermore, in ITER, the limited penetration of recycling neutrals into the pedestal region is expected to result in a weaker density gradient, which in turn increases the $\eta_e$ and $\eta_i$ parameters in the pedestal region and thereby enhances the drive for $\eta_e$-TEM and ion temperature gradient instabilities. Given the anticipated lower density gradient, reduced $\mathrm{E}\times\mathrm{B}$ shear, and lower collisionality in the ITER pedestal, the excitation of the $\eta_e$-TEM is expected to be further facilitated, making this pedestal regime a promising candidate for the ITER and future reactors.

*Acknowledgments*—We thank the EAST team for their support of the experiment, providing data, analysis, and related simulations presented in this article. Numerical computations were performed at the Hefei advanced computing center. The work was supported by the National Magnetic Confinement Fusion Energy Program of China under Grant No. 2019YFE03030000.

G. S. X. and G. F. D. are co-first authors.

*Data availability*—The data that support the findings of this article are openly available [36]; embargo periods may apply.

[1] A. Loarte *et al.*, Plasma Phys. Controlled Fusion **67**, 065023 (2025).
[2] F. Reimold, M. Wischmeier, M. Bernert, S. Potzel, A. Kallenbach, H. W. Müller, B. Sieglin, and U. Stroth, Nucl. Fusion **55**, 033004 (2015).
[3] D. Eldon *et al.*, Nucl. Fusion **57**, 066039 (2017).
[4] F. Wagner *et al.*, Phys. Rev. Lett. **49**, 1408 (1982).
[5] A. W. Leonard, Phys. Plasmas **21**, 090501 (2014).

[6] E. Viezzer, Nucl. Fusion **58**, 115002 (2018).
[7] A. Kallenbach *et al.*, Nucl. Fusion **61**, 016002 (2021).
[8] M. Bernert *et al.*, Nucl. Fusion **61**, 024001 (2021).
[9] L. Wang *et al.*, Nat. Commun. **12**, 1365 (2021).
[10] D. G. Wu *et al.*, Nucl. Fusion **64**, 086042 (2024).
[11] S. Glöggler *et al.*, Nucl. Fusion **59**, 126031 (2019).
[12] B. G. Wang *et al.*, Nucl. Fusion **65**, 086004 (2025).
[13] P. Barabaschi *et al.*, Fusion Eng. Des. **215**, 114990 (2024).
[14] H. Q. Wang *et al.*, Phys. Rev. Lett. **112**, 185004 (2014).
[15] G. S. Xu *et al.*, Rev. Mod. Plasma Phys. **7**, 14 (2023).
[16] J. Y. Kim and H. S. Han, Phys. Plasmas **24**, 072501 (2017).
[17] C. Giroud *et al.*, in *Proceeding of the 30th IAEA Fusion Energy Conference, Chengdu, China, 2025* (IAEA, Vienna, 2025), paper IAEA-CN-316/2924, https://conferences.iaea.org/event/392/contributions/35673/attachments/19737/36117/Giroud_paper_EX_C_iaea2025_6.pdf.
[18] Y. R. Martin *et al.*, *J. Phys. Conf. Ser.* 123, 012033 (2008).
[19] K. Wu *et al.*, Plasma Phys. Controlled Fusion **63**, 105004 (2021).
[20] M. F. Wu *et al.*, J. Instrum. **15**, P12009 (2020).
[21] G. S. Xu *et al.*, Nucl. Fusion **60**, 086001 (2020).
[22] G. S. Xu *et al.*, Nucl. Fusion **61**, 126070 (2021).
[23] K. Verhaegh *et al.*, Nucl. Fusion **59**, 126038 (2019).
[24] C. Zhou *et al.*, Rev. Sci. Instrum. **84**, 103511 (2013).
[25] P. B. Snyder, H. R. Wilson, J. R. Ferron, L. L. Lao, A. W. Leonard, T. H. Osborne, A. D. Turnbull, D. Mossessian, M. Murakami, and X. Q. Xu, Phys. Plasmas **9**, 2037 (2002).
[26] X. Q. Xu, B. Dudson, P. B. Snyder, M. V. Umansky, and H. Wilson, Phys. Rev. Lett. **105**, 175005 (2010).
[27] See Supplemental Material at http://link.aps.org/supplemental/10.1103/7r3f-dqft for setup and input profiles used for the GENE simulations, which includes Refs. [28–32].
[28] F. Jenko, W. Dorland, M. Kotschenreuther, and B. N. Rogers, Phys. Plasmas **7**, 1904 (2000).
[29] T. Görler *et al.*, J. Comput. Phys. **18**, 230 (2011).
[30] H. John, T. S. Taylor, Y. R. Lin-Liu, and A. D. Turnbull, Transport simulation of negative magnetic shear discharges No. GA-A–21847; IAEA-CN–60/DD-II-8; CONF-940933–20 (General Atomics, San Diego, CA, USA, 1994).
[31] O. Sauter, C. Angioni, and Y. R. Lin-Liu, Phys. Plasmas **6**, 2834 (1999).
[32] J. Candy, Plasma Phys. Controlled Fusion **51**, 105009 (2009).
[33] K. D. Li *et al.*, Nucl. Fusion **63**, 026025 (2023).
[34] M. Kotschenreuther, D. R. Hatch, S. Mahajan, P. Valanju, L. Zheng, and X. Liu, Nucl. Fusion **57**, 064001 (2017).
[35] D. R. Ernst *et al.*, in *Proceedings of the 27th IAEA Fusion Energy Conference, Gandhinagar, India, 2018* (IAEA, Vienna, 2018), paper IAEA-CN-258/EX/2-2, https://nucleus.iaea.org/sites/fusionportal/Shared%20Documents/FEC%202018/fec2018-preprints/preprint0580.pdf.
[36] G. S. Xu, Zenodo, 2026, 10.5281/zenodo.18697543.
[37] J. Candy, E. A. Belli, and R. V. Bravenec, Comput. Phys. **324**, 73 (2016).
[38] Sun Hee Kim and Tom Casper, ITER-IO, File output from CORSICA integrated modeling code for running H-mode13 at 00400s on October 19, 2017, Associated EQDSK file name is G_HMODE13_ITER_MR_00400.TXT.
[39] P. B. Snyder, R.J. Groebner, J. W. Hughes, T. H. Osborne, M. Beurskens, A. W. Leonard, H. R. Wilson, and X.Q. Xu, Nucl. Fusion **51**, 103016 (2011).

## End Matter

*Gyrokinetic simulations of HFBT in the EAST pedestal using the GENE code*—The experimentally measured profiles during the $N_2$ seeding at 6.15 s of the discharge No. 133903 and the magnetic equilibrium calculated by high-resolution kinetic equilibrium fitting code [32] are used as input for the GENE simulations. The gyrokinetic calculation was performed at $\psi_N = 0.98$ in the pedestal gradient region where the HFBT was observed based on the MPCR measurement. The linear simulation result (Fig. 5) indicates that the $\eta_e$-TEM is the dominant mode in the HFBT wave number range of $k_y\rho_s = 0.6$–$1.2$ during $N_2$ seeding, where $\eta_e = \partial_r \ln T_e/\partial_r \ln n_e$. The mode propagates in the electron diamagnetic drift direction with a frequency of about 50–100 kHz. Taking into account the Doppler shift $f_{E\times B} \sim 400$ kHz, the mode frequency in laboratory frame is $f_{\rm lab} = 450$–$500$ kHz, consistent with the observed HFBT frequency. The mode structure shows typical characteristics of a TEM: (1) the electrostatic potential, $\phi(\theta)$, features an even-parity structure [Fig. 2(c)]. (2) The parallel magnetic vector potential, $A_\parallel(\theta)$, features an odd-parity structure with a normalized amplitude much lower than that of the electrostatic potential [Fig. 5(d)], consistent with the electrostatic mode characteristic observed in the experiment. The growth rate of this mode increases with $\eta_e$ and decreases with $\nu_e^*$ [Figs. 5(d) and 5(f)], suggesting that the mode is destabilized by the $T_e$ gradient and stabilized by collisionality, again in good agreement with the experimental observations. In addition, a nonlinear simulation was performed to assess the transport characteristics of the HFBT. The nonlinear flux spectra [Fig. 5(h)] suggest that the $\eta_e$-TEM dominates the fluxes, driving significant outward electrostatic electron heat and particle fluxes, where the spectra are extracted from the saturation phase $t \sim 40$–$100 a/c_s$ [Fig. 5(g)]. Here, $a$ is the minor radius. The electron heat and particle fluxes peak at $k_y\rho_s \sim 0.7$–$0.9$, consistent with the experimental observation of HFBT at $k_y\rho_s \sim 0.85$.

*Predictions of ITER pedestal turbulence mode using GENE and CGYRO*—We carried out gyrokinetic simulations of the pedestal gradient region of the ITER baseline scenario with $I_p = 15$ MA using GENE and CGYRO codes [36]. The profile data of the ITER $I_p = 15$ MA baseline scenario was generated by the CORSICA integrated modeling code [37] with the pedestal

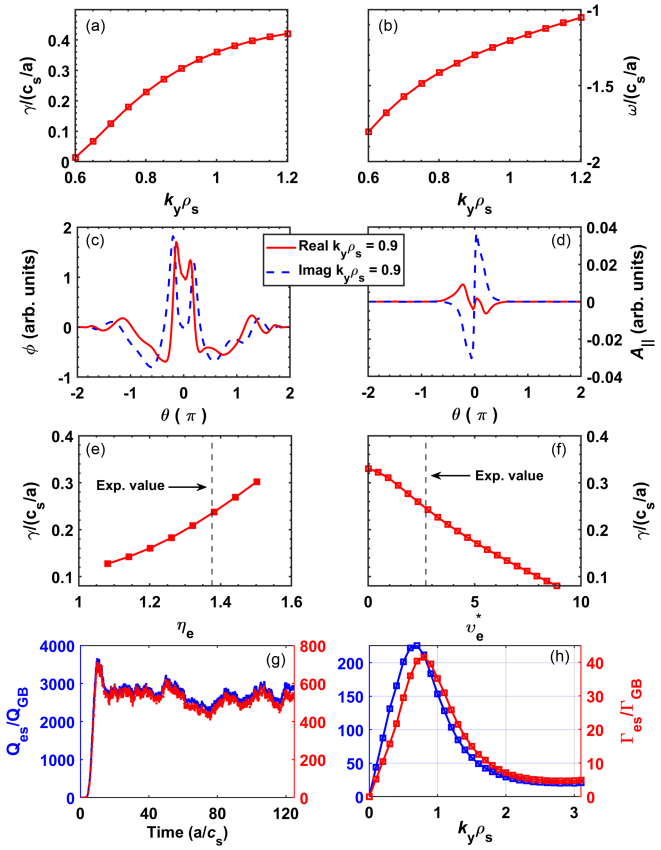



FIG. 5. (a) Linear growth rate and (b) real frequency normalized by $c_s/a$ as a function of $k_y\rho_s$. The real and imaginary parts of the (c) electrostatic potential and (d) parallel magnetic vector potential eigenfunctions as a function of the extended ballooning angle $\theta$ at $k_y\rho_s = 0.9$. Growth rate vs $\eta_e$ (e) and $\nu_e^*$ (f). (g) Real time trace of the electron heat (blue) and particle (red) flux. (h) Electron heat (blue) and particle (red) flux spectra extracted from the saturation phase $t \sim 40$–$100a/c_s$.

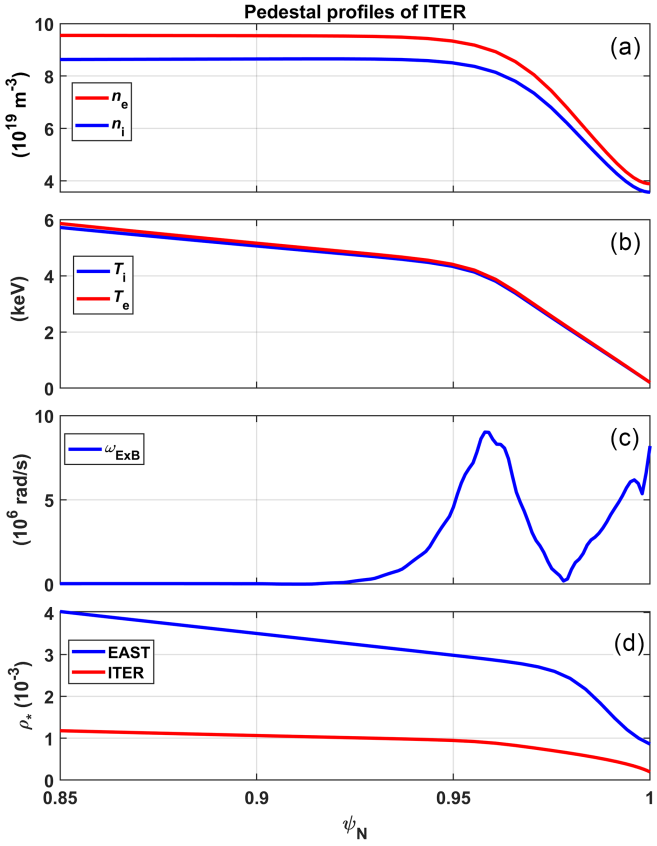



FIG. 6. Pedestal profiles of the ITER $I_p = 15$ MA baseline scenario. Pedestal profiles of (a) electron density (red) and main ion density (blue), (b) electron (red) and ion (blue) temperature, (c) E × B shearing rate $\omega_{E\times B}$, (d) normalized ion gyroradius $\rho^*$ of the ITER (red) and the EAST (blue).

constructed based on the edge pedestal model prediction [38,39]. The ITER pedestal profiles used for GENE and CGYRO simulations are shown in Fig. 6.

Both the GENE and CGYRO simulations exhibit the similar results, as shown in Fig. 7. In the intermediate $k_y\rho_s$ range, 0.3–2, there is a mode propagating in the electron diamagnetic drift direction with a linear growth rate well above the local E × B shearing rate (as indicated by the dashed line). The normalized parallel magnetic vector potential, $A_\parallel(\theta)$, of the mode at $k_y\rho_s = 0.6$, is significantly smaller than that of the electrostatic potential, $\phi(\theta)$, suggesting it is in an electrostatic mode. In order to identify the mode, we scan the temperature gradients, $a/L_{Te}$. The growth rate increases linearly with $a/L_{Te}$, suggesting it being a $\eta_e$-TEM. Therefore, Both the GENE and CGYRO simulation results suggest that the $\eta_e$-TEM can be excited in the pedestal steep-gradient region under the projected ITER conditions.

*Implementation prospects of the DTP regime on the ITER*—For future fusion reactors, such as the ITER, $P_{sep}$ is typically designed to be only slightly greater than the $P_{L-H}$ to minimize the challenges posed by divertor heat

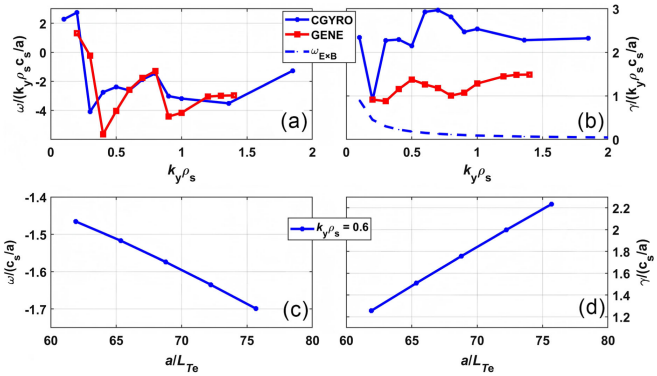



FIG. 7. Simulation of linear modes in the ITER pedestal gradient region using GENE (red) and CGYRO (blue). (a) Real frequency and (b) linear growth rate normalized by $k_y\rho_s c_s/a$ as a function of $k_y\rho_s$. Scans of $a/L_{Te}$ at $k_y\rho_s = 0.6$ show (c) real frequency and (d) linear growth rate normalized by $c_s/a$, respectively.

loads, just like in the selected case of the EAST discharge No. 133903. Even with marginal heating power, significant enhancement in the pedestal performance can be achieved with the DTP regime.

Nitrogen effectively established the regime in the EAST. However, it is not a suitable seeding impurity for the ITER. Although it exhibits good radiation efficiency in the low-temperature divertor and benefits from strong impurity screening, nitrogen chemically reacts with tungsten and hydrogen isotopes, increasing tritium retention and potentially forming ammonialike compounds that would complicate fuel processing. Consequently, an alternative impurity such as neon, whose radiation can be well-confined within the ITER's higher-temperature divertor, would likely be required to fulfill the same physics function. Thus, while the specific impurity may change, the underlying DTP physics offers a promising pathway toward stationary, high-performance fusion plasmas in a full-metal wall environment.